ACS Catalysis

pubs.acs.org/acscatalysis Research Article

Enzymatic C3-Methylation of Indoles Using Methyltransferase PsmD—Crystal Structure, Catalytic Mechanism, and Preparative Applications

Diana A. Amariei, Nadiia Pozhydaieva, Benoit David, Pascal Schneider, Thomas Classen, Holger Gohlke, Oliver H. Weiergräber, and Jörg Pietruszka*

Cite This: *ACS Catal.* 2022, 12, 14130−14139 Read Online

ACCESS | Metrics & More | Article Recommendations | Supporting Information

ABSTRACT: Enantioselective methylation is a challenging task in organic chemistry, yet often desirable in drug discovery and optimization. *S*-Adenosyl methionine (SAM)-dependent methyltransferases (MTases) offer a selective alternative to chemical synthesis and an abundance of potential scaffolds. The crystal structure of C3-indole MTase PsmD from *Streptomyces griseofuscus*, involved in the biosynthesis of the acetylcholinesterase inhibitor physostigmine, was determined via X-ray crystallography. The amino acid residues essential for catalysis were identified by site-directed mutagenesis, and a mechanism of action was proposed. Furthermore, a PsmD ortholog was identified and characterized. The variant catalyzed enantioselective C-methylation over a broad substrate scope while displaying increased stability. Using this enzyme, preparative-scale enzymatic methylation was performed in cell-free extracts in combination with an SAM recycling system, eliminating the need for cofactor supplementation.

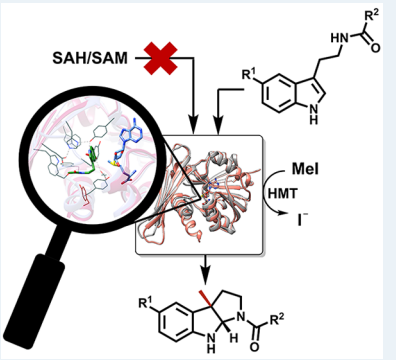

KEYWORDS: *methyltransferase, physostigmine, protein structures, SAM recycling, reaction mechanism, acetylcholinesterase inhibitors, C-methylation*

INTRODUCTION

C−C bond formation is a key aspect of organic chemistry and a ubiquitous process in biology. In living organisms, the addition of a single carbon in the form of the methyl group is among the most abundant reactions in secondary metabolism.[1,2] Addition of a methyl group to small molecules is now considered a conventional approach for modulating their biological activity.[3] Methylation can drastically affect the target compound's biological and biophysical properties, such as stability, solubility, and bioactivity. Such effects underline the general interest for efficient methylation strategies in organic synthesis and particularly in drug development.[2,4] Stereo- and regioselective methylation is generally challenging for chemical synthesis and, if at all possible, usually involves toxic reagents and complex catalysts.[5] Therefore, the shift to biocatalytic selective methylation is a promising direction toward effective synthetic strategies for methylated compounds.[6,7]

S-Adenosyl-L-methionine (SAM)-dependent methyltransferases (MTases) are widely distributed over all natural systems. They target a wide spectrum of biological molecules and are involved in biosynthesis, genetic regulation, and molecular signaling. They generally transfer a methyl group from the SAM cofactor to nucleophiles from a large variety of target molecules via an S_N2-type mechanism.[1,7] So far, five structural classes of SAM-dependent MTases have been described, covering a major subset of folds identified in SAM-binding enzymes in general.[8,9]

Although SAM is the most common methyl donor in nature, the use of SAM-dependent MTases in biocatalysis remains limited due to the reduced availability and the high cost of the cofactor.[7,10,11] SAM production in vivo has been optimized using metabolic engineering, and so far large-scale processes involving MTases have been performed in vivo.[12] On the other hand, SAM production in situ and SAM recycling systems provide valuable tools for in vitro biocatalysis involving MTases. The natural metabolic cycle for SAM regeneration involves six different enzymes and has been successfully reconstituted in vitro.[13] However, the large-scale application of such a complex system remains a challenge. Supply systems for SAM have been developed as well, the most prominent using methionine adenosyl transferases (MATs) for SAM production starting from methionine and ATP.[14] More recently, a recycling system was proposed based on halide methyltransferases (HMTs), using methyl iodide (MeI) for the

Received: August 26, 2022
Revised: October 18, 2022
Published: November 3, 2022

regeneration of SAM from *S*-adenosyl homocysteine (SAH) in a single step.[15] This system has been further developed for producing various alkylated cofactors through directed evolution and identification of new HMT variants.[16,17] Access to efficient cofactor recycling systems leads to new opportunities in the use and development of small-molecule MTases for preparative-scale synthesis.

Bioactive alkaloids, in particular pyrroloindoles, are a group of natural compounds that have attracted considerable interest in recent years due to their prevalence as medicinal agents (Figure 1).[18−23] More generally, the indole scaffold is an

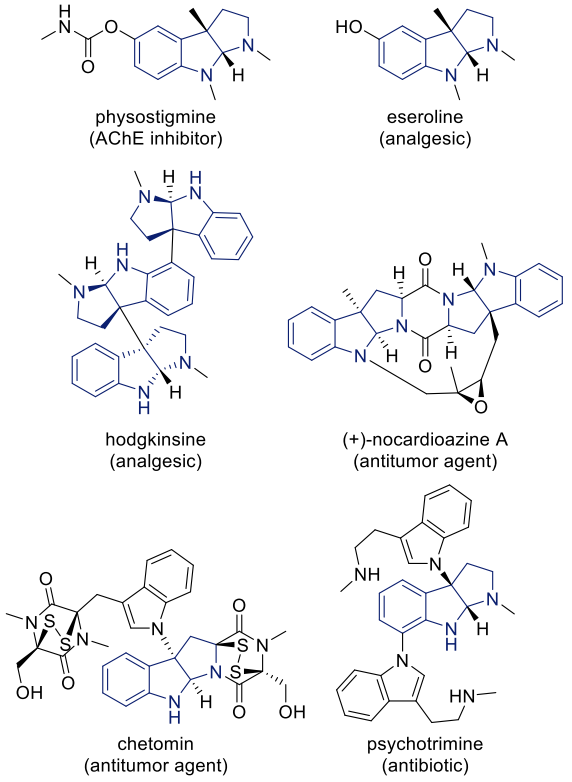

Figure 1. Representative bioactive alkaloids containing the pyrroloindole motif.

abundant motif in natural products with biological activity, justifying the current interest in its structural diversification.[24] Physostigmine is a natural product of *Physostigma venenosum* known for its effect as an acetylcholine esterase (AChE) inhibitor. Its therapeutic applications involve the treatment of Alzheimer's disease and glaucoma and the reversal of anticholinergic poisoning.[25,26]

Physostigmine has been industrially produced by *Streptomyces griseofuscus*.[27] Its biosynthetic gene cluster has been identified, and the enzyme responsible for the enantioselective indole C3-methylation (PsmD_*Sg*) was characterized.[28,29] In this work, the structure of PsmD_*Sg* was elucidated via X-ray crystallography and a mechanism of action is proposed, based on the mutagenesis of candidate catalytic residues. Additionally, a homologous gene cluster was identified in *Streptomyces albulus*, and a new PsmD variant (PsmD_*Sa*) was expressed and characterized. Several advantages of PsmD_*Sa* compared to PsmD_*Sg* were observed concerning biophysical and biochemical properties. Enzymatic methylation was performed on a preparative scale using a HMT-based cofactor recycling system, demonstrating its applicability for large-scale synthesis. PsmD_*Sa* exhibits a high potential for application in biocatalysis for the synthesis of diverse pyrroloindole derivatives.

RESULTS AND DISCUSSION

PsmD_*Sa* is located in a gene cluster homologous to the one responsible for physostigmine production in *S. griseofuscus* (NRRL 5324).[28] PsmD orthologs exhibit 90% amino acid sequence identity (Figure S1). Interestingly, however, no physostigmine production has been reported so far in *S. albulus*. Due to the high sequence similarity, [3-(2-acetamidoethyl)-1*H*-indol-5-yl] *N*-methylcarbamate (**1**) has been assumed to be the natural substrate for PsmD_*Sa* (Scheme 1), as it is for its homolog. A synthetic gene coding for PsmD_*Sa* was cloned in a pET21a(+) vector including a C-terminal His_6-tag and expressed in *E.coli* BL21 Gold (DE3).

Scheme 1. Reaction Catalyzed by SAM-Dependent PsmD

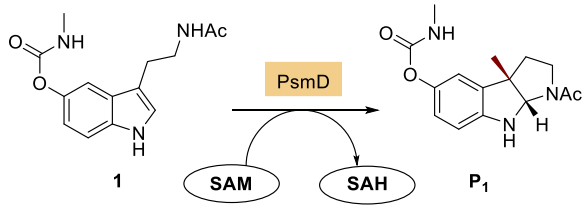

Biochemical Characterization of PsmD_*Sa*. PsmD_*Sa* was purified and further characterized with respect to its biocatalytic properties (Figure 2). A temperature screening was

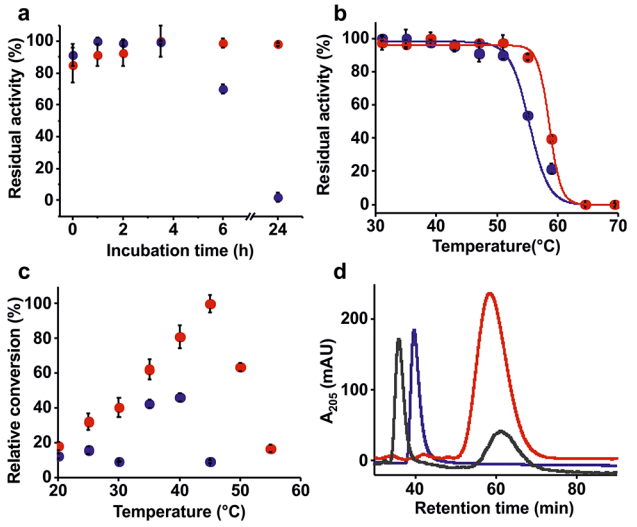

Figure 2. Biochemical characterization of PsmD_*Sa* (red) and PsmD_*Sg* (blue). (a) Activity over time at 35 °C. (b) Thermal inactivation (fitting parameters in SI). (c) Conversion as a function of temperature. (d) Chiral HPLC chromatogram showing substrate **1** (blue), racemic standard **P1** (gray), and the **P1** enantiomer obtained from the PsmD_*Sa* reaction (red).

performed in a range of 20 to 55 °C. Psmd_*Sa* performs better than its homolog PsmD_*Sg* at higher temperatures, with an optimum at 45 °C (Figure 2c). A higher optimal temperature suggests greater thermostability, which was confirmed by a difference in the thermal inactivation temperature between the two enzymes: PsmD_*Sa* displays a thermal melting transition at 58.6 °C, as opposed to 55.3 °C for PsmD_*Sg* (Figure 2b).

https://doi.org/10.1021/acscatal.2c04240
ACS Catal. 2022, 12, 14130−14139

Table 1. Kinetic Parameters of PsmD_*Sa* and PsmD_*Sg*

	substrate	V_{max} (μmol × min^{-1} × g$_{enz}^{-1}$)[a]	K_M (μM)[a]	k_{cat} (min^{-1})[b]	k_{cat}/K_M (μM^{-1} × min^{-1})[b]
PsmD_*Sa*	1	6.1 ± 0.4	14.5 ± 3.1	0.19 ± 0.01	(13 ± 3.7) × 10^{-3}
	SAM	5.5 ± 0.2	16.8 ± 2.2	0.18 ± 0.01	(10 ± 1.8) × 10^{-3}
PsmD_*Sg*	1	18.3 ± 0.4	11.3 ± 1.1	0.54 ± 0,01	(93 ± 14.9) × 10^{-3}
	SAM	11.2 ± 0.4	6.6 ± 0.6	0.36 ± 0.01	(54 ± 7.0) × 10^{-3}

[a]Errors from least-square fitting including replicates. [b]Errors result from error propagation.

Significant difference in stability over time was observed as well; PsmD_*Sg* starts losing activity after 4 h at 35 °C and is essentially inactive after 24 h, while PsmD_*Sa* activity remains unchanged under the same conditions (Figure 2a). Both enzymes show optimal activity in the pH range of 6−8 (Figure S14).[29] The enantioselectivity of the reaction catalyzed by PsmD_*Sa* was determined using normal-phase chiral high-performance liquid chromatography (HPLC). Biotransformations were performed using a cell lysate containing the overexpressed PsmD_*Sa*, and product formation was analyzed. The enzyme's stereoselective activity toward the presumed natural substrate is apparent when compared to the racemic standard (Figure 2d). Comparing the kinetic parameters at 35 °C for the two enzymes, there are notable differences. Psmd_*Sg* displays a higher turnover number and catalytic efficiency (Table 1). However, PsmD_*Sa* provides better overall performance under the same conditions due to its increased stability, which outweighs the kinetic disadvantage, eventually leading to higher overall yields.

Psmd Reaction Using a SAM Recycling System. Methylations were performed in the presence of an SAM recycling system involving an HMT from *Chloracidobacterium thermophilum*. The two proteins were expressed in the *E. coli* SAH-nucleosidase-deficient strain Δmtn (DE3).[15] The recycling system performed well in the preliminary experiments using the two enzymes directly in lysate; therefore, the optimization of the process was performed using a four-factor central composite design of experiment. The variable parameters were the volumes of the two cell-free extracts (PsmD and HMT), as well as MeI and SAH concentrations. The screening was performed using 1 mM of substrate **1**, with optimal parameters listed in Figure 3. The results show a small influence of the amount of HMT lysate present in the mixture, the quantity of PsmD lysate being the limiting factor for the conversion (Figure S15). Interestingly, we observed that the supplementation of SAH does not influence the productivity of the system. It thus appears that the residual SAH present in the cell-free extract is enough for the cascade to perform at full rate. Due to the high cost of the SAH cofactor, circumventing the need for supplying it provides a very attractive perspective for the potential large-scale application of the system. We also observed that MeI shows an inhibitory effect at high concentrations, as well as causing *N*-methylation of the product when present in high excess. The highest conversion in the coupled system was obtained at 35 °C (Figure S17). Having determined the optimal conditions for the coupled reactions, the system was scaled up to 100 mg of substrate **1**. After 16 h of incubation at 35 °C, the substrate was fully converted. The procedure provided an enantiomeric excess (*ee*) > 99%, and we obtained 54% yield for the isolated C-methylated product. Low amounts of N-methylated product were detected (approx. 5% of the product). All the controls containing **P1** and methylating agents (SAM or MeI) led to N-methylation. As such, although nonselective methylation by PsmD cannot be ruled out completely, we attributed the presence of the side product most likely to the background methylation of the product **P1**.

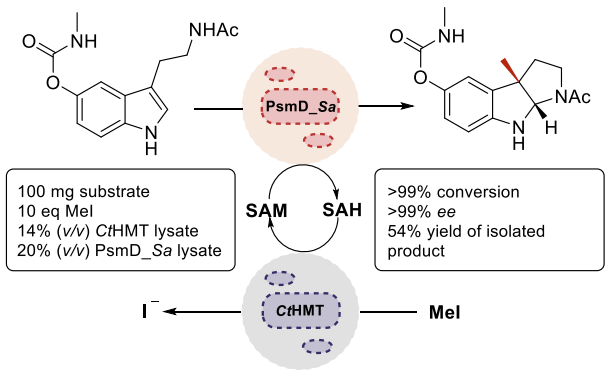

Figure 3. Representation of the coupled methylation system and the optimal composition of the reaction mixture.

A range of substrates were tested for conversion using the commercial *MTase Glo assay* (Promega), which allows for SAH detection and quantification via a luminescence reaction.[30] The resulting trend in specific activities was consistent with the results reported for PsmD_*Sg*.[29] The SAH production rate was evaluated after 15 min of reaction. It was observed that bulky residues hindered enzymatic activity on both the carbamate and amide functionalities (Figure 4).

Furthermore, substrates derivatized in other positions on the phenyl ring led to significant activity reduction. Substrates lacking side chains (**12**−**18**), especially on the carbamate side (including melatonin **12**), also provided low activity with both enzymes.

Structural Aspects. Dynamic light scattering measurements were performed to probe the quaternary structure of the two PsmD variants. While PsmD_*Sa* displayed a largely monodisperse distribution consistent with a dimeric species, data for PsmD_*Sg* indicated fractional aggregation of the protein under the same conditions. Gel filtration analysis (Figure S25) and mass photometry (Figure S27) confirmed that both proteins exhibit a dimeric form under usual experimental conditions. In order to obtain insight into the three-dimensional structure and the potential catalytic mechanism of PsmD, we set out to crystallize both variants of the enzyme in the absence or presence of the cofactor SAM.

Crystals were obtained for all four combinations (PsmD_*Sa*/PsmD_*Sg*; apo/SAH). In contrast to PsmD_*Sg* samples, however, those of the *S. albulus* ortholog could not be optimized to yield high-resolution diffraction datasets within the scope of this study. Since PsmD_*Sg* was observed to crystallize in two different space groups in the presence of the cofactor, a total of three structures were determined (refer to Table S4 for data collection and refinement statistics); unless indicated otherwise, structural features will be discussed using

https://doi.org/10.1021/acscatal.2c04240
ACS Catal. 2022, 12, 14130−14139

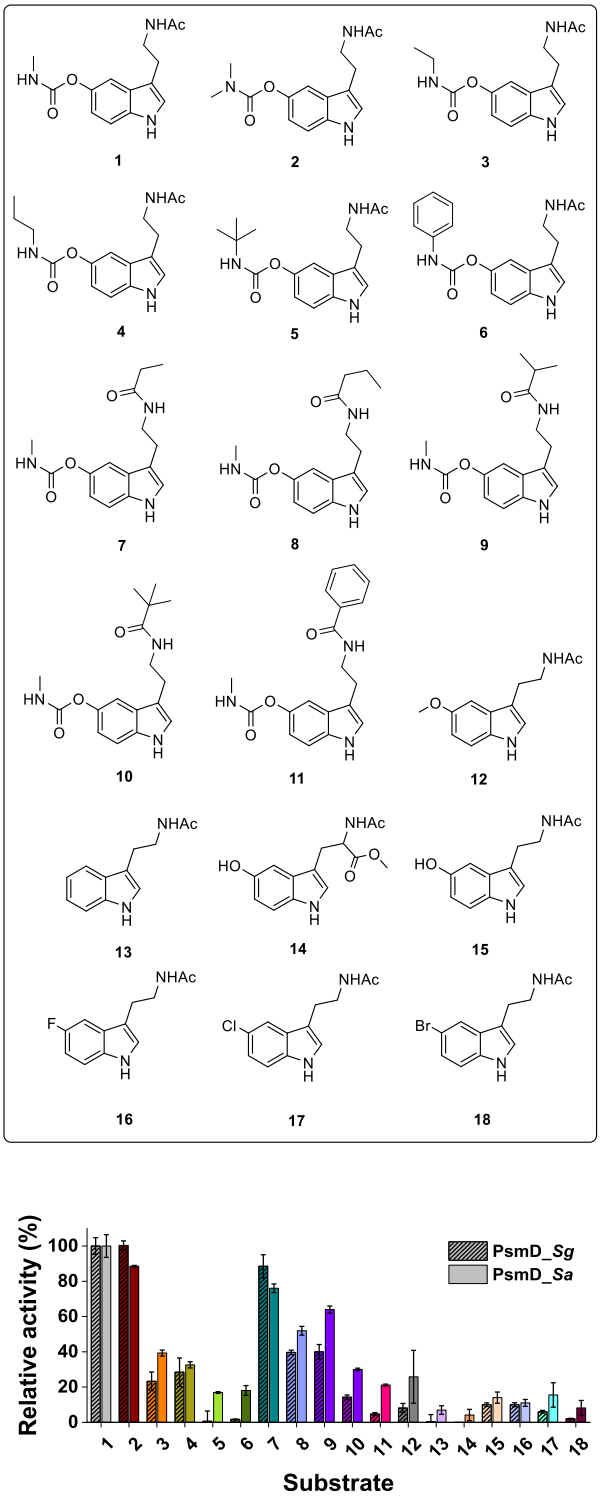

Figure 4. Substrate scope and relative activities of PsmD_*Sg* and PsmD_*Sa*.

crystal form 1 of the PsmD−SAH complex. PsmD features a variant Rossmann fold characteristic of class-I SAM-dependent MTases, that is, a central mostly parallel β-sheet flanked by α-helices on either side (Figure 5a). A remarkable feature of the PsmD structure is an additional four-stranded antiparallel β-sheet (strands $\beta1'$ through $\beta4'$) inserted between strand $\beta5$ and helix αE of the Rossmann fold, which we term the β-cap domain. This portion of the molecule not only plays a fundamental role in catalysis (discussed below) but also acts as a dimerization domain. Crystals of the apo protein as well as form-2 crystals of the complex contain two copies per asymmetric unit, which interact in essentially the same way, while in form-1 crystals, an analogous dimer is generated by crystallographic symmetry (Figure 5b). The β-sheets cross at a right angle, burying a roughly square area of the solvent-accessible surface [approx. 790 and 660 Å^2 per chain for the apo protein and the cofactor complex, respectively, as determined by PISA (Proteins, Interfaces, Structures, and Assemblies)].[31] At the center of the interface, the F201 side chains of both molecules engage in a staggered π-stack with one another and an orthogonal interaction with Y211 (Figure 5c). This aromatic cluster is complemented by additional hydrophobic interactions and a pronounced network of hydrogen bonds and salt bridges at the periphery. While PISA classifies this assembly as metastable, the organization of the interface and its consistent appearance under very different crystallization conditions indicate that the dimer is significant in solution, in accordance with other experimental evidence.

Together with an N-terminal extension containing helix αA′, the β-cap domain confines a solvent-filled cavity containing the catalytic center (Figure 6a). The bottom of the cavity harbors the binding site for the cofactor. As observed in other families of Rossmann-fold proteins, the first $\beta\alpha\beta$ element plays an essential role in coordinating the nucleotide cofactor with a GTG motif at positions 66−68 in the $\beta1$-αB loop, allowing for a sharp bend into helix αB beneath the SAM molecule, and an aspartic acid residue (D85) at the end of strand $\beta2$, forming hydrogen bonds with the ribose hydroxyl groups (Figure 6b). We note that the cofactor is consistently present as *S*-adenosyl-L-homocysteine (SAH), indicating that it has been turned over by the enzyme. Similar to the ribose, the homocysteine moiety of SAH is involved in extensive polar interactions with the enzyme, including a salt bridge of its carboxyl group with R39 and several hydrogen bonds mediated, for example, by hydroxyl groups of Y23 and T123 as well as by the main-chain carbonyl of C64. Lastly, the adenine ring is inserted in a largely apolar pocket, where it is sandwiched between the side chain of C64 and the aliphatic portion of R86 and receives additional van der Waals contacts by M2, L109, and Y129. At the same time, three of its nitrogen atoms are engaged in hydrogen bonds with the PsmD main chain. Note that the cofactor is covered by a cluster of tyrosine residues (Y16, Y23, and Y129, contacting the ribose, homocysteine, and adenine moieties, respectively), which is further stabilized by the M90 side chain. The central layer of the catalytic cavity (Figure 6c) contains some disordered solvent, and the lateral walls are essentially polar and include a glutamic acid−histidine pair (E216/H218 on strand $\beta4'$ of the β-cap domain), which may be part of a proton-relay system (discussed below). Finally, the catalytic pocket features an intriguing density of aromatic side chains projecting from the β-cap domain toward the cavity (Figure 6d). It is important to note that the N-terminal segment preceding helix αA′ (highlighted in dark green in Figures 5 and 6) is disordered in the apo protein but well ordered in crystal form 1 of the SAH complex, effectively acting as a lid obturating the entrance to the catalytic cavity. Henceforth, we will be therefore referring to the conformational states represented by the apo and form 1 complex structures as the open and closed states, respectively. In the closed state, the lid region is affixed to both domains of the protein via a dense network of polar and nonpolar interactions

https://doi.org/10.1021/acscatal.2c04240
ACS Catal. 2022, 12, 14130−14139

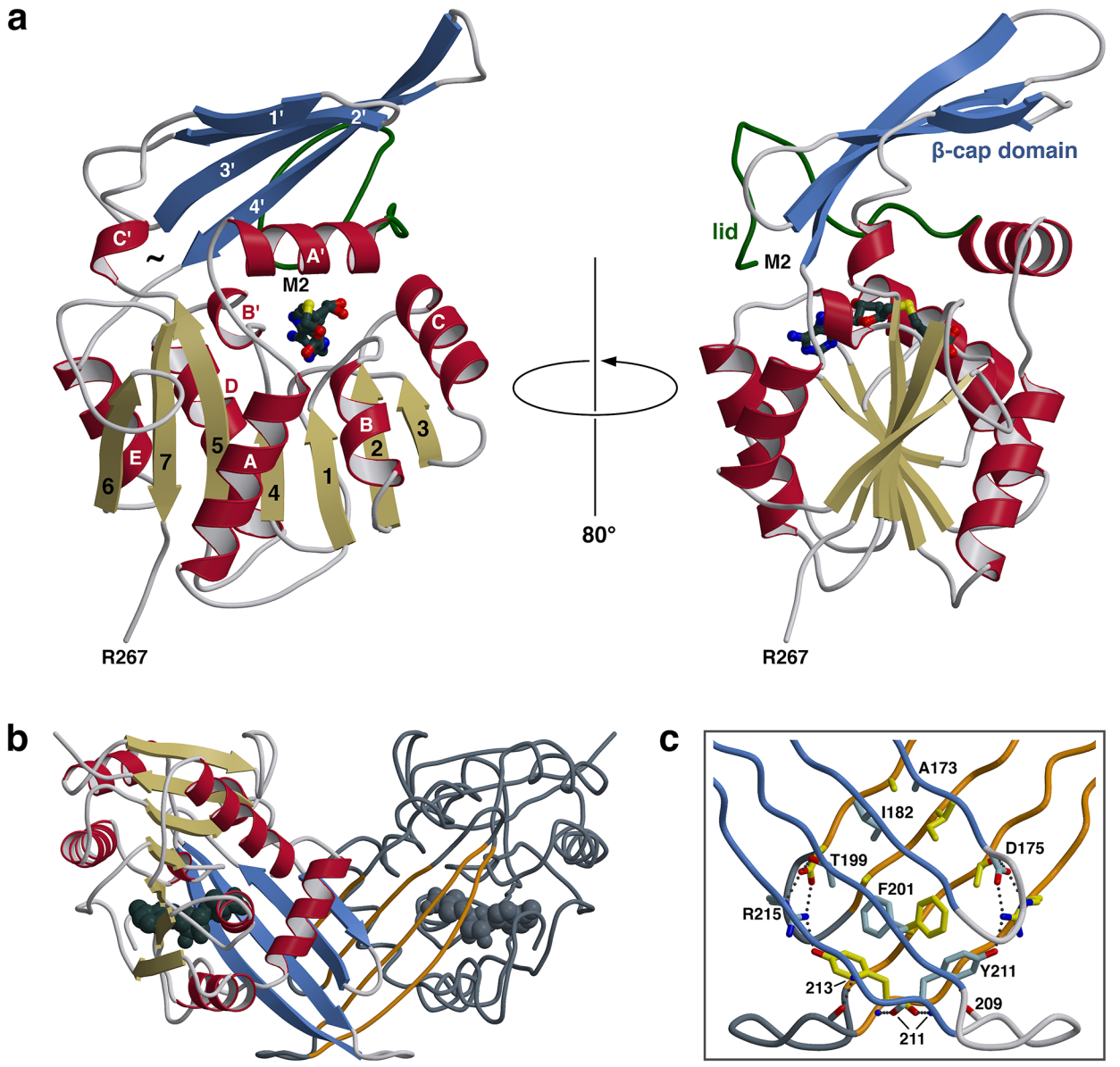

Figure 5. X-ray structure of PsmD_*Sg* in complex with SAH (crystal form 1). (a) Ribbon representation showing the two-domain architecture, comprising a Rossmann-type α/β fold (red/gold) and an all-β domain termed the β-cap (blue). Helices and strands are labeled by upper case letters and numbers, respectively, using a prime symbol for elements outside the core Rossmann fold. The active center, as indicated by the cofactor (ball-and-stick model), is located at the interface between the two domains and is laterally bounded by an N-terminal extension containing helix A′ as well as the lid region (dark green). A tilde symbol marks a highly dynamic region which may operate as a gate for the reaction product. (b) Dimeric arrangement mediated by the β-cap domain, as found in all PsmD_*Sg* crystal forms. The symmetry mate is drawn in coil mode, with the β-cap strands highlighted in orange. (c) Close-up view of the dimerization interface. For visual clarity, residues are labeled in the primary copy only.

(Figure 6c). It seems reasonable to assume that, upon binding to the enzyme, the cofactor molecule initially nucleates the tyrosine cluster in its immediate vicinity, involving recruitment of Y16 in the proximal lid along with a roughly 120° flip of the Y23 side chain and moderate adjustment of Y129.

Once triggered, the assembly of the entire network may proceed in a highly cooperative manner. The β-cap domain, specifically the strand $\beta4'$, contributes several residues to this machinery, with E216 and H218 linking the tyrosine cluster to residues 16−19 of the lid. The result is a precisely defined orientation of side chains on the inner walls of the closed catalytic cavity. It is intriguing to note that crystal form 2 of the PsmD_*Sg*−SAH complex presents a disordered lid region (similar to the apo enzyme) and a distinctly different SAH conformation compared to crystal form 1. These observations indicate that the two PsmD_*Sg*-SAH crystal forms sample distinct states of the catalytic cycle (discussed in more detail below).

Mechanistic Analysis. Due to challenging cloning and expression of PsmD_*Sg*, its ortholog PsmD_*Sa* was used for in-depth evaluation of potential catalytic site residues (note the offset of −1 in sequence positions). Molecular docking of substrate **1** onto a PsmD_*Sa* homology model in a closed conformation, followed by molecular dynamics (MD) simulations, revealed two potential poses that are consistent with the stereochemistry of the methyl transfer reaction catalyzed by PsmD (Scheme 2).[29]

https://doi.org/10.1021/acscatal.2c04240
ACS Catal. 2022, 12, 14130−14139

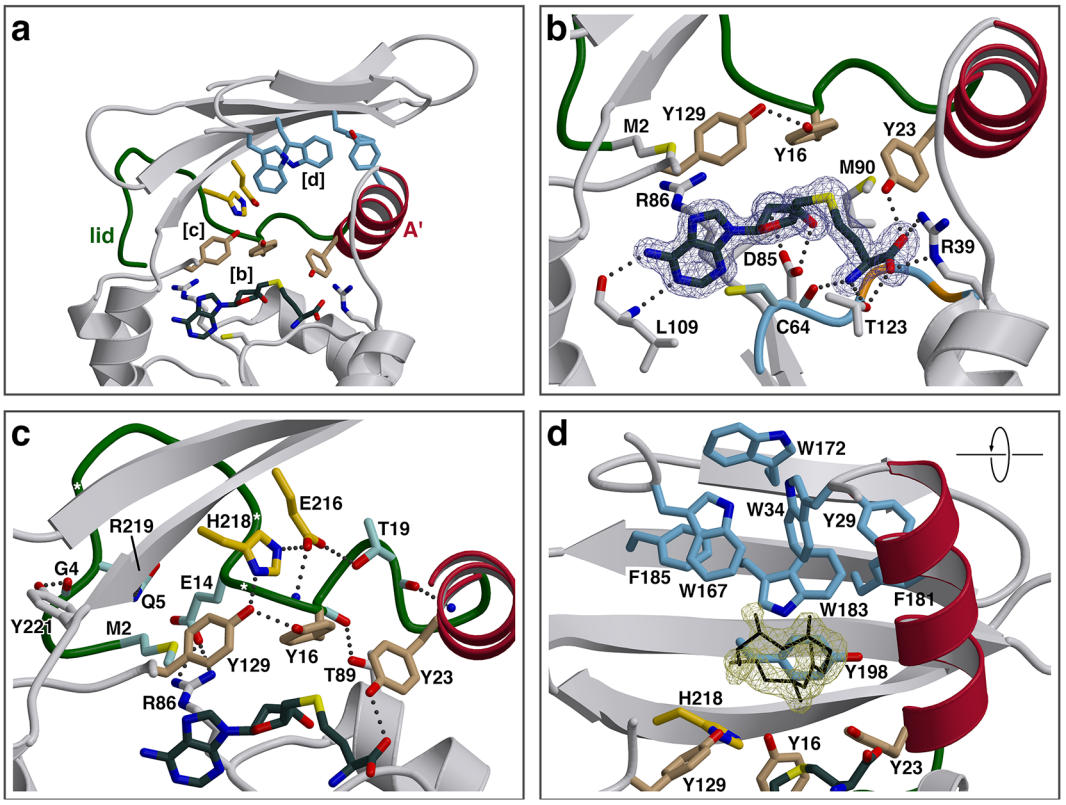

Figure 6. Active-site cavity of PsmD_*Sg* (SAH complex, crystal form 1). (a) Overview revealing a layered architecture, featuring (from bottom to top) the docked cofactor (dark gray), a tyrosine cluster (light brown) connected to a presumed proton-relay system (gold), and a second aromatic cluster (blue). Lower case letters refer to the close-up views in subsequent panels. (b) Environment of the cofactor. In the β1-αB loop forming the base of the pocket, glycine residues of the GTG motif (positions 66 and 68) are highlighted in orange. (c) Interactions fixing the lid region (dark green) in the closed state. White asterisks indicate the positions of proline residues supporting the central bulge. (d) Aromatic cluster at the bottom surface of the β-cap domain. The black skeleton represents an unidentified molecule, which is probably derived from the bacterial expression host. Electron densities ($2mF_o$-DF_c) are contoured at 1 rmsd for SAH and at 0.9 rmsd for the unknown ligand.

The orientation of the docked substrate in pose 1 strongly supports the interpretation of Y128, E215, and H217, placed in close proximity to each other and at the methylation site, as a catalytic triad responsible for the electronic activation of the substrate via an acid−base mechanism. Specifically, we suggest that Y128 is deprotonated through a Glu-His-Tyr proton shuttle system. Variations of this system were reported in other MTases, with a histidine residue often present as a general base, in some cases accompanied by activating acidic residues.[1,32−34] Similarly, catalytic dyads containing adjacent histidine and tyrosine residues have been reported in several MTases that display an acid−base mechanism of activation prior to methylation.[35−37] In PsmD, the negatively charged Y128 is suggested to activate the substrate by engaging the proton attached to the indole nitrogen, increasing the electron density on the indole ring and triggering the nucleophilic attack of C3 on the methyl group of SAM (Scheme 2a). Substrate activation could be achieved via hydrogen bonding or deprotonation by the Y128 phenolate anion. By analogy with chemical methylation of substrate **1**, which requires prior activation with a strong base, the enzymatic reaction could likely involve deprotonation, where Y128 assumes the role of the base.[38]

An alanine scan was performed on PsmD_*Sa* to determine amino acid residues essential for substrate binding and catalysis. The variants were used in whole cells to determine substrate conversion to the product after 16 h. The mutant Y128A lost all activity, while E215A and H217A retained less than 15% activity compared to the wild type, providing strong arguments for the importance of these residues in the catalytic process (Table 2).

In contrast to pose 1, pose 2 is mainly stabilized by a hydrogen bond between the substrate indole nitrogen and the carboxylate of E35 (Scheme 2b). Due to the presumed role of the Glu-His-Tyr proton shuttle, we propose pose 1 as the functional position of the substrate and will refer to this arrangement in the further discussion. However, pose 2 cannot be excluded and is evaluated in detail in the Supporting Information.

While some of the selected residues led to a loss of activity upon substitution with alanine, E157A catalyzed almost full conversion, and T18A, M89A, and R85A converted approximately half of the substrate. The mutant E35A led to 5% conversion. In pose 1, the importance of residue E35 could be attributed to substrate binding, as it forms a hydrogen bond with the carbamate nitrogen. Such an interaction could also reasonably explain the observed importance of the carbamate moiety in the structures of the accepted substrates. Y128A lost all activity, confirming the relevance of this tyrosine, while Y128F led to 11% conversion of the substrate. The latter observation suggests a steric effect of Y128, besides its putative role in substrate activation. As encountered in other MTases with an acid−base mechanism of action, H217 or a water

https://doi.org/10.1021/acscatal.2c04240
ACS Catal. 2022, 12, 14130−14139

Scheme 2. View of Both Substrate Docking Poses in the PsmD_*Sa* Active Site (Taken from Snapshots Extracted from the MD Simulations of the Closed Conformation) and the Proposed Mechanisms of Methylation and Subsequent Intramolecular Cyclization for Each Case[a]

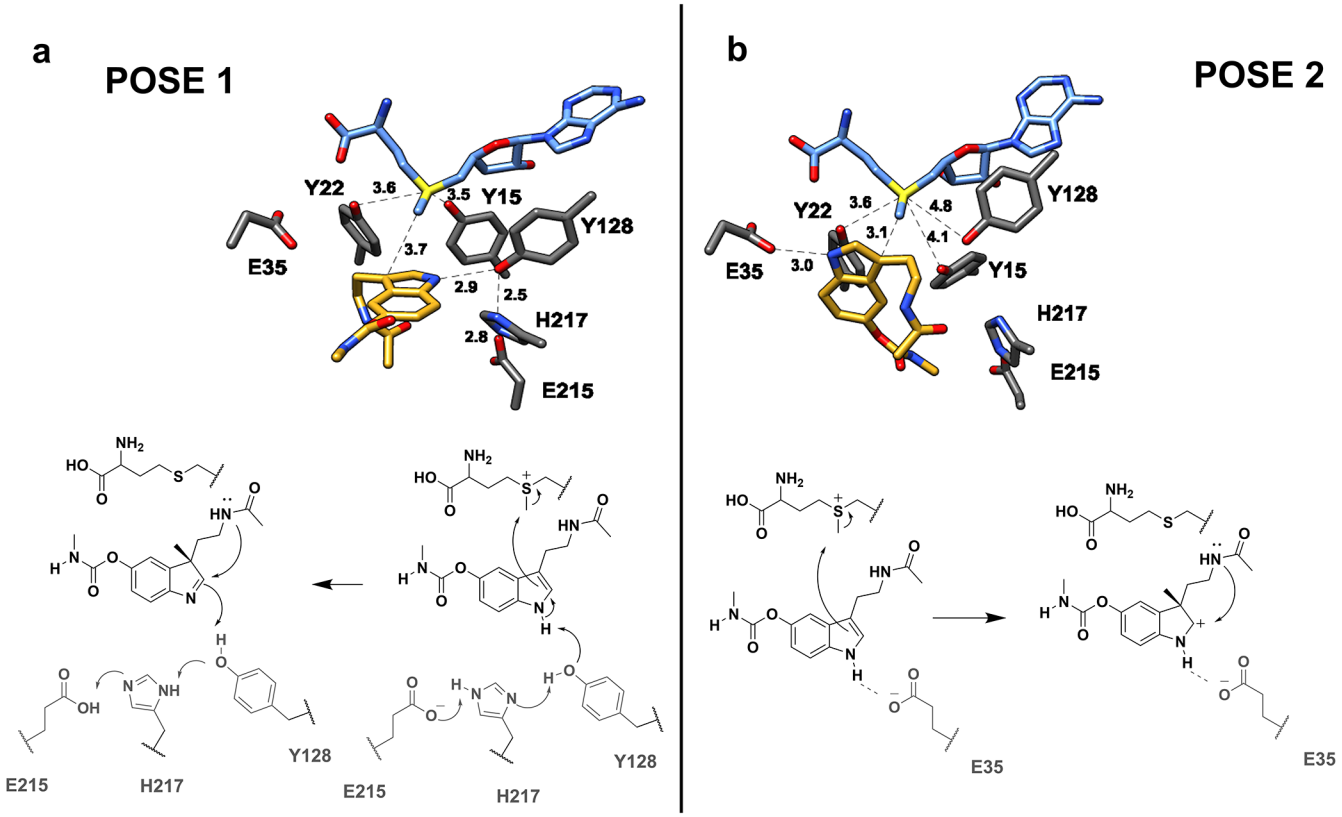

[a](a) Substrate docking pose 1. (b) Substrate docking pose 2. The carbon atoms of the substrate and the SAM cofactor are colored in gold and blue, respectively. Dashed lines illustrate relevant distances with the surrounding active site residues.

Table 2. Conversion (%) of Substrate 1 by the Tested PsmD_*Sa* Mutants[a]

Y15A (Y16)	Y15F (Y16)	T18A (T19)	Y22A (Y23)	Y22F (Y23)	E35A (E36)
R38A (R39)	D84A (D85)	R85A (R86)	M89A (M90)	Y128A (Y129)	Y128F (Y129)
E157A (E158)	E215A (E216)	E215D (E216)	H217A (H218)	WT	EV

0 10 20 30 40 50 60 70 80 90 100

[a]The conversion was measured via reverse phase (RP)-HPLC, after 16 h of reaction time. WT: wild type PsmD_*Sa*; EV: pET21a(+) empty vector control. The corresponding amino acid positions in PsmD_*Sg* are displayed in parentheses.

molecule could play the base role in the absence of Y128 phenol, albeit in this case with a significant decrease in activity.

Residue Y15 seems to play an important role in the catalytic process; our crystal structures of PsmD_*Sg* indicate that, by virtue of its polar and aromatic properties, it could participate in at least three distinct processes: binding of the cofactor, positioning of the catalytic residue Y128 (together with H217 and E215), and closure of the lid. Upon replacing Y15 with alanine, all of these activities are abolished, and the enzyme is inactivated. However, full conversion was achieved with the mutant Y15F, indicating that either hydrogen bonding to Y128 is not essential or the π-electron system of F15 assumes the role of a hydrogen bond acceptor. Replacing residue Y22 with alanine led to complete loss of activity, while Y22F yielded as much as 66% conversion after 16 h of reaction. This hints at an important function of the aromatic residue, which only partly depends on its hydroxyl group. As evidenced by the Psmd_*Sg* crystal structures, this tyrosine residue drastically changes its side-chain orientation in the closed form of the enzyme, with its hydroxyl group hydrogen-bonded to the cofactor's carboxylate and the aromatic ring complementing the hydrophobic environment (Figures 6 and 7A). Crystal form 2 of the PsmD_*Sg*−SAH complex, featuring an open conformation, is particularly interesting in this context since the absence of the Y23-SAH (Y22 in PsmD_*Sa*) contact correlates with a remarkably different conformation of the cofactor. When the methyl group is added in silico to SAH to yield SAM in the naturally occurring (S)-configuration, it is pointing away from the substrate (Figure 7A). These observations indicate that a fundamental role of Y22 in the catalytic process could involve the proper orientation of the cofactor for the methylation reaction. The associated adjustment of Y22, in turn, may favor establishment of the dense network of interactions driving closure of the lid (Figure 6).

Based on the above considerations, we suggest that the closed state represented by crystal form 1 of the SAH complex approximates a situation in which both the substrate/product and cofactor are present in the catalytic center. In the open-lid

https://doi.org/10.1021/acscatal.2c04240
ACS Catal. 2022, 12, 14130−14139

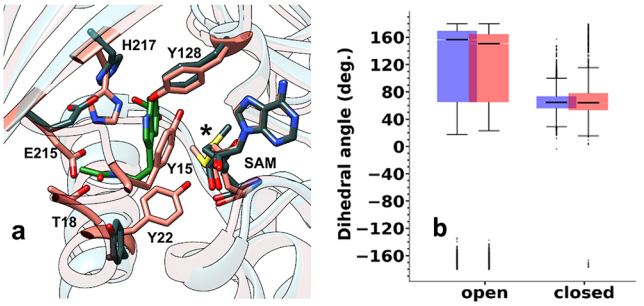

Figure 7. Significance of the Y22 residue. (a) Location of Y22 in relation to SAM in the open (gray) and closed (pink) conformations of the PsmD_*Sa* homology model. The substrate (green) is represented in docking pose 1. The SAM cofactor (methyl group marked by asterisk) was modeled based on the position of SAH in the respective crystal structure of each conformation in PsmD_*Sg*. (b) Influence of the conformation (open/closed) of the N-terminal lid (blue: substrate pose 1; red: substrate pose 2) on the fluctuations of the Y22 Cα-Cβ torsion angle over the course of the simulations.

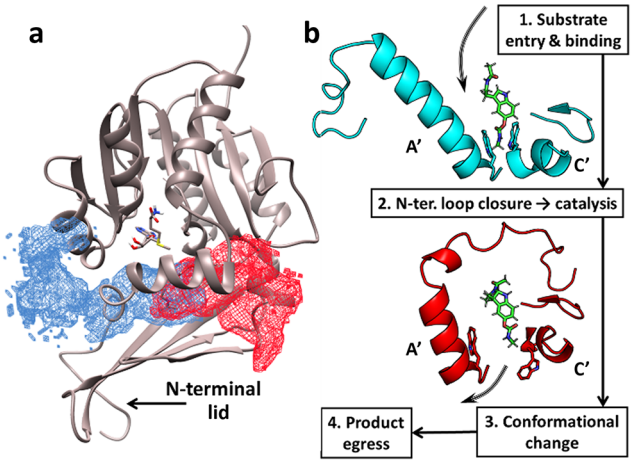

Figure 8. Consequences of the conformational state of the N-terminal lid on the dynamics of the substrate (calculated from the simulations including the substrate pose 1). (a) Computed volume occupied by the substrate indole ring during the simulations of the PsmD_*Sa* dimer in complex with both SAM and substrate. Both open (blue mesh) and closed (red mesh) states were simulated. The SAM cofactor is represented in sticks. The structure of PsmD in its closed state is shown in the gray cartoon. (b) Proposed product egress mechanism. The impact of both opening (blue) and closing (red) conformations of the N-terminal lid on adjacent structural motifs and on the orientation of W33 and W166 side chains is shown.

structure found in crystal form 2 of the complex, the nonproductively oriented cofactor might represent SAH just prior to release but could also hint at the conformation of SAM waiting to be locked into its final position, the latter possibly triggered by the substrate in the physiological setting. A conformational change of SAM/SAH after the catalytic process was reported before for TrmD tRNA *N*-methyltransferase.[39] In the course of the reaction cycle, the lid may serve a regulatory role by controlling access to substrates and release of products to/from the catalytic cavity, thus minimizing the generation of potentially toxic side products and preventing the loss of costly intermediates. Similar N-terminal lids have been found in other MTases such as Nov-P, MycF, and TylF.[40,41]

Besides this gate-keeping role of the N-terminal lid region, our structural analysis points to direct conformational cross-talk with the catalytic site, chiefly mediated by the tyrosine cluster covering the cofactor. For obtaining deeper insight into these interdependencies, a comparative analysis of the MD simulation trajectories of the dimeric PsmD_*Sa* homology model in both open and closed conformations was performed. Simulations in the presence of both substrate poses revealed a particularly high mobility of the Y22 side chain in the open conformation as opposed to the closed conformation (Figure 7B). Given the conservation of Y22 in MTase homologs (Figure S33) and its interaction with both the substrate and SAM in the closed state (Scheme 2, Figure S34), it is conceivable that stabilization of its side chain is essential to promote PsmD activity. We suggest that Y22, Y15, and potentially Y128 could contribute to the formation of a partially negatively charged area, which may stabilize the positively charged sulfonium ion of SAM, triggering the productive conformation of the cofactor. Such a general role of Y22 and Y15 beyond the particular PsmD reaction mechanism is implied by the recurrence of similar tyrosine residues in the structures of other MTases catalyzing a diverse range of reactions.[33−35,42,43] Moreover, principal component analysis (Figure S36) revealed that the closure of the N-terminal lid triggers the opening of a channel at the opposing side of the protein through which the departure of the substrate was observed after approximately 100 ns in all simulation replicas (Figure 8). This opening motion, during which either α-helices A′ and C′ move apart (Figure 8, S38A−S39) or the β-sheet adjacent to the Rossmann fold twists (Figures S37−S38B), could plausibly allow the reaction product to exit the enzyme once the reaction is performed. This interpretation is supported by our crystallographic data: the structure of closed-state Psmd_*Sg* (Figure 5) features remarkable mobility in this region, involving alternate conformations of the helix C′ backbone and several bulky aromatic side chains lining the putative gate. We thus propose that the closure of the N-terminal lid is not only essential for organizing the active site electrostatic environment prior to catalysis but also for product egress.

CONCLUSIONS

The new PsmD variant described in this work, PsmD_*Sa*, provides a more robust alternative for the late-stage enantioselective methylation of physostigmine precursors due to its increased stability. The enzymatic reaction could be scaled up using an HMT-based SAM recycling system without any cofactor supplementation, granting a promising potential for cost-efficient, large-scale enzymatic C-methylation. The crystal structure of PsmD_*Sg* combined with the alanine scan of the catalytic pocket and in silico docking of the natural substrate reveals two possible mechanisms of action, based on substrate electronic activation by a Glu-His-Tyr proton shuttle. We also observed various conformational changes of the protein and the cofactor, likely occurring upon substrate binding and catalysis. The structural and mechanistic information reported in this work contributes to a better understanding of the PsmD structure−function relationship, paving the way for substrate diversification through protein engineering.

https://doi.org/10.1021/acscatal.2c04240
ACS Catal. 2022, 12, 14130−14139

■ ASSOCIATED CONTENT

Supporting Information

The Supporting Information is available free of charge at https://pubs.acs.org/doi/10.1021/acscatal.2c04240.

Additional experimental details, materials, and methods, including ^{1}H NMR data and HPLC chromatograms (PDF)

■ AUTHOR INFORMATION

Corresponding Author

Jörg Pietruszka − *Institute of Bioorganic Chemistry & Bioeconomy Science Center (BioSC), Heinrich Heine University Düsseldorf in Forschungszentrum Jülich, Jülich 52426, Germany; Institute of Bio- and Geosciences (IBG-1: Bioorganic Chemistry) & Bioeconomy Science Center (BioSC) Forschungszentrum Jülich, Jülich 52426, Germany;* orcid.org/0000-0002-9819-889X; Email: j.pietruszka@fz-juelich.de

Authors

Diana A. Amariei − *Institute of Bioorganic Chemistry & Bioeconomy Science Center (BioSC), Heinrich Heine University Düsseldorf in Forschungszentrum Jülich, Jülich 52426, Germany*

Nadiia Pozhydaieva − *Institute of Bioorganic Chemistry & Bioeconomy Science Center (BioSC), Heinrich Heine University Düsseldorf in Forschungszentrum Jülich, Jülich 52426, Germany;* orcid.org/0000-0003-2468-4235

Benoit David − *Institute of Bio- and Geosciences (IBG-4: Bioinformatics), Forschungszentrum Jülich, Jülich 52426, Germany*

Pascal Schneider − *Institute of Bioorganic Chemistry & Bioeconomy Science Center (BioSC), Heinrich Heine University Düsseldorf in Forschungszentrum Jülich, Jülich 52426, Germany*

Thomas Classen − *Institute of Bio- and Geosciences (IBG-1: Bioorganic Chemistry) & Bioeconomy Science Center (BioSC) Forschungszentrum Jülich, Jülich 52426, Germany;* orcid.org/0000-0002-3259-964X

Holger Gohlke − *Institute of Bio- and Geosciences (IBG-4: Bioinformatics), Forschungszentrum Jülich, Jülich 52426, Germany; Institute for Pharmaceutical and Medicinal Chemistry & Bioeconomy Science Center (BioSC), Heinrich Heine University Düsseldorf, Düsseldorf 40225, Germany*

Oliver H. Weiergräber − *Institute of Biological Information Processing (IBI-7: Structural Biochemistry) & Jülich Centre for Structural Biology (JuStruct), Forschungszentrum Jülich, Jülich 52425, Germany*

Complete contact information is available at: https://pubs.acs.org/10.1021/acscatal.2c04240

Author Contributions

The manuscript was written through contributions of all authors. All authors have given approval to the final version of the manuscript.

Notes

The authors declare no competing financial interest.

■ ACKNOWLEDGMENTS

Dedicated to Karl-Erich Jaeger for his pioneering contributions in the field of molecular enzyme technology. We gratefully acknowledge the state of North Rhine Westphalia (NRW) and the European Regional Development Fund (EFRE) for funding the project within the "CLIB-Kompetenzzentrum Biotechnologie," grant numbers 34-EFRE-0300096 and 34-EFRE-0300097 as well as the German Federal Ministry of Education of Research (BMBF, "Modellregion, BioRevierPlus: BioökonomieREVIER Innovationscluster Biotechnologie & Kunststofftechnik—BioTech", grant number 031B1134A) and the Heinrich Heine University Düsseldorf and the Forschungszentrum Jülich GmbH for their ongoing support. We acknowledge DESY (Hamburg, Germany), a member of the Helmholtz Association HGF, for the provision of experimental facilities. Part of this research was carried out at PETRA III, and we would like to thank Dr. J. Hakanpää for assistance in using beamline P11. B.D. and H.G. gratefully acknowledge the computational support provided by the Center for Information and Media Technology at the Heinrich Heine University Düsseldorf and the computing time provided by the John von Neumann Institute for Computing on the supercomputer JURECA at Jülich Supercomputing Centre (project: VSK33). We are grateful to Dr. Georg Hochberg (MPI Marburg) for the opportunity to perform mass photometry analysis and to Dr. Jan Schuller (Phillips University, Marburg) for the opportunity to run analytical SEC.

■ ABBREVIATIONS

SAM: *S*-adenosyl-L-methionine; SAH: *S*-adenosyl-L-homocysteine; MAT: methionine adenosyl transferase; HMT: halide methyltransferase; SEC: size-exclusion chromatography

■ REFERENCES

(1) Liscombe, D. K.; Louie, G. V.; Noel, J. P. Architectures, Mechanisms and Molecular Evolution of Natural Product Methyltransferases. *Nat. Prod. Rep.* **2012**, *29*, 1238−1250.

(2) Schönherr, H.; Cernak, T. Profound Methyl Effects in Drug Discovery and a Call for New C-H Methylation Reactions. *Angew. Chem., Int. Ed.* **2013**, *52*, 12256−12267.

(3) Barreiro, E. J.; Kümmerle, A. E.; Fraga, C. A. M. The Methylation Effect in Medicinal Chemistry. *Chem. Rev.* **2011**, *111*, 5215−5246.

(4) Leung, C. S.; Leung, S. S. F.; Tirado-Rives, J.; Jorgensen, W. L. Methyl Effects on Protein − Ligand Binding. *J. Med. Chem.* **2012**, *55*, 4489−4500.

(5) Aynetdinova, D.; Callens, M. C.; Hicks, H. B.; Poh, C. Y. X.; Shennan, B. D. A.; Boyd, A. M.; Lim, Z. H.; Leitch, J. A.; Dixon, D. J. Installing the "Magic Methyl" − C − H Methylation in Synthesis. *Chem. Soc. Rev.* **2021**, *50*, 5517−5563.

(6) Bennett, M. R.; Shepherd, S. A.; Cronin, V. A.; Micklefield, J. Recent Advances in Methyltransferase Biocatalysis. *Curr. Opin. Chem. Biol.* **2017**, *37*, 97−106.

(7) Struck, A.-W.; Thompson, M. L.; Wong, L. S.; Micklefield, J. S-Adenosyl-Methionine-Dependent Methyltransferases: Highly Versatile Enzymes in Biocatalysis, Biosynthesis and Other Biotechnological Applications. *Chembiochem* **2012**, *13*, 2642−2655.

(8) Kozbial, P. Z.; Mushegian, A. R. Natural History of S -Adenosylmethionine-Binding Proteins. *BMC Struct. Biol.* **2005**, *5*, 1−26.

(9) Schubert, H. L.; Blumenthal, R. M.; Cheng, X. Many Paths to Methyltransfer : A Chronicle of Convergence. *Trends Biochem. Sci.* **2003**, *28*, 329−335.

(10) Mordhorst, S.; Andexer, J. N. Round, Round We Go − Strategies for Enzymatic Cofactor Regeneration. *Nat. Prod. Rep.* **2020**, *37*, 1316−1333.

(11) Micklefield, J. Streamlined Recycling of S -Adenosylmethionine. *Nat. Catal.* **2019**, *2*, 644−645.

(12) Kunjapur, A. M.; Hyun, J. C.; Prather, K. L. J. Deregulation of S-Adenosylmethionine Biosynthesis and Regeneration Improves Methylation in the E . Coli de Novo Vanillin Biosynthesis Pathway. *Microb. Cell Factories* **2016**, *15*, 1−17.
(13) Mordhorst, S.; Siegrist, J.; Müller, M.; Richter, M.; Andexer, J. N. Catalytic Alkylation Using a CyclicS-Adenosylmethionine Regeneration System. *Angew. Chem. Int. Ed.* **2017**, *56*, 4037−4041.
(14) Singh, S.; Zhang, J.; Huber, T. D.; Sunkara, M.; Hurley, K.; Goff, R. D.; Wang, G.; Zhang, W.; Liu, C.; Rohr, J.; Van Lanen, S. G.; Morris, A. J.; Thorson, J. S. Facile Chemoenzymatic Strategies for the Synthesis and Utilization of S-Adenosyl-L-Methionine Analogues. *Angew. Chem. Int. Ed.* **2014**, *53*, 3965−3969.
(15) Liao, C.; Seebeck, F. P. S. Adenosylhomocysteine as a Methyl Transfer Catalyst in Biocatalytic Methylation Reactions. *Nat. Catal.* **2019**, *2*, 696−701.
(16) Tang, Q.; Grathwol, C. W.; Aslan-Üzel, A. S.; Wu, S.; Link, A.; Pavlidis, I. V.; Badenhorst, C. P. S.; Bornscheuer, U. T. Directed Evolution of a Halide Methyltransferase Enables Biocatalytic Synthesis of Diverse SAM Analogs. *Angew. Chem. Int. Ed.* **2021**, *60*, 1524−1527.
(17) Tang, Q.; Pavlidis, I. V.; Badenhorst, C. P. S.; Bornscheuer, U. T. From Natural Methylation to Versatile Alkylations Using Halide Methyltransferases. *Chembiochem* **2021**, *22*, 2584−2590.
(18) Li, H.; Qiu, Y.; Guo, C.; Han, M.; Zhou, Y.; Feng, Y.; Luo, S.; Tong, Y.; Zheng, G.; Zhu, S. Pyrroloindoline Cyclization in Tryptophan- Containing Cyclodipeptides Mediated by an Unprecedented Indole C3 Methyltransferase from Streptomyces Sp. HPH0547. *Chem. Commun.* **2019**, *55*, 8390−8393.
(19) Raju, R.; Piggott, A. M.; Huang, X.-C.; Capon, R. J. A Novel Bridged Diketopiperazine Scaffold from a Marine-Derived Bacterium Inhibits P-Glycoprotein. *Org. Lett.* **2011**, *13*, 2770−2773.
(20) Viziteu, E.; Grandmougin, C.; Goldschmidt, H.; Seckinger, A.; Hose, D.; Klein, B.; Moreaux, J. Chetomin, Targeting HIF-1α/P300 Complex, Exhibits Antitumour Activity in Multiple Myeloma. *Br. J. Cancer* **2016**, *114*, 519−523.
(21) Galli, A.; Renzi, G.; Grazzini, E.; Bartolini, R.; Aiello-Malmberg, P.; Bartolini, A. Reversible Inhibition of Acetylcholinesterase by Eseroline, an Opioid Agonist Structurally Related to Physostigmine (Eserine) and Morphine. *Biochem. Pharmacol.* **1982**, *31*, 1233−1238.
(22) Amador, T. A.; Verotta, L.; Nunes, D. S.; Elisabetsky, E. Antinociceptive Profile of Hodgkinsine. *Planta Med.* **2000**, *66*, 770−772.
(23) Schallenberger, M. A.; Newhouse, T.; Baran, P. S.; Romesberg, F. E. The Psychotrimine Natural Products Have Antibacterial Activity against Gram-Positive Bacteria and Act via Membrane Disruption. *J. Antibiot.* **2010**, *63*, 685−687.
(24) Kaushik, N. K.; Kaushik, N.; Attri, P.; Kumar, N.; Kim, C. H.; Verma, A. K.; Choi, E. H. Biomedical Importance of Indoles. *Molecules* **2013**, *18*, 6620−6662.
(25) Davis, K. L.; Mohs, R. C.; Tinklenberg, J. R.; Pfefferbaum, A.; Hollister, L. E.; Kopell, B. S. Physostigmine: Improvement of Long-Term Memory Processes in Normal Humans. *Science* **1978**, *201*, 272−274.
(26) Triggle, D. J.; Mitchell, J. M.; Filler, R. The Pharmacology of Physostigmine. *CNS Drug Rev* **1998**, *4*, 87−136.
(27) Zhang, J.; Martin, C.; Shifflet, M. A.; Salmon, P.; Brix, T.; Greasham, R.; Buckland, B.; Chartrain, M. Development of a Defined Medium Fermentation Process for Physostigmine Production by Streptomyces Griseofuscus. *Appl. Microbiol. Biotechnol.* **1996**, *44*, 568−575.
(28) Liu, J.; Ng, T.; Rui, Z.; Ad, O.; Zhang, W. Unusual Acetylation-Dependent Reaction Cascade in the Biosynthesis of the Pyrroloindole Drug Physostigmine. *Angew. Chem. Int. Ed.* **2014**, *53*, 136−139.
(29) Schneider, P.; Henßen, B.; Paschold, B.; Chapple, B. P.; Schatton, M.; Seebeck, F. P.; Classen, T.; Pietruszka, J. Biocatalytic C3-Indole Methylation — A Useful Tool for the Natural-Product-Inspired Stereoselective Synthesis of Pyrroloindoles. *Angew. Chem. Int. Ed.* **2021**, *60*, 23412−23418.
(30) Hsiao, K.; Zegzouti, H.; Goueli, S. A. Methyltransferase-Glo: A Universal , Bioluminescent and Homogenous Assay for Monitoring All Classes of Methyltransferases. *Epigenomics* **2016**, *8*, 321−339.
(31) Krissinel, E.; Henrick, K. Inference of Macromolecular Assemblies from Crystalline State. *J. Mol. Biol.* **2007**, *372*, 774−797.
(32) Zubieta, C.; He, X.; Dixon, R. A.; Noel, J. P. Structures of Two Natural Product Methyltransferases Reveal the Basis for Substrate Specificity in Plant O-Methyltransferases. *Nat. Struct. Biol.* **2001**, *8*, 271−279.
(33) Lang, D. E.; Morris, J. S.; Rowley, M.; Torres, M. A.; Maksimovich, V. A.; Facchini, P. J.; Ng, K. K. S. Structure−Function Studies of Tetrahydroprotoberberine N-Methyltransferase Reveal the Molecular Basis of Stereoselective Substrate Recognition. *J. Biol. Chem.* **2019**, *294*, 14482−14498.
(34) Zhang, X.; Zhou, L.; Cheng, X. Crystal Structure of the Conserved Core of Protein Arginine Methyltransferase PRMT3. *EMBO J.* **2000**, *19*, 3509−3519.
(35) Lee, S. G.; Kim, Y.; Alpert, T. D.; Nagata, A.; Jez, J. M. Structure and Reaction Mechanism of Phosphoethanolamine Methyltransferase from the Malaria Parasite Plasmodium Falciparum. *J. Biol. Chem.* **2012**, *287*, 1426−1434.
(36) Takata, Y.; Huang, Y.; Komoto, J.; Yamada, T.; Konishi, K.; Ogawa, H.; Gomi, T.; Fujioka, M.; Takusagawa, F. Catalytic Mechanism of Glycine N-Methyltransferase,. *Biochemistry* **2003**, *42*, 8394−8402.
(37) Lemfack, M. C.; Brandt, W.; Krüger, K.; Gurowietz, A.; Djifack, J.; Jung, J.-P.; Hopf, M.; Noack, H.; Junker, B.; von Reuß, S.; Piechulla, B. Reaction Mechanism of the Farnesyl Pyrophosphate C -Methyltransferase towards the Biosynthesis of Pre-Sodorifen Pyrophosphate by Serratia Plymuthica 4Rx13. *Sci. Rep.* **2021**, *11*, 1−13.
(38) Yi, J.-C.; Liu, C.; Dai, L.-X.; You, S.-L. Synthesis of C3-Methyl-Substituted Pyrroloindolines and Furoindolines via Cascade Dearomatization of Indole Derivatives with Methyl Iodide. *Chem.−Asian J.* **2017**, *12*, 2975−2979.
(39) Ahn, H. J.; Kim, H.; Yoon, H.; Lee, B. I.; Suh, S. W.; Yang, J. K. Crystal Structure of TRNA (M1G37) Methyltransferase: Insights into TRNA Recognition. *EMBO J.* **2003**, *22*, 2593−2603.
(40) Gómez García, I.; Stevenson, C. E. M.; Usón, I.; Freel Meyers, C. L.; Walsh, C. T.; Lawson, D. M. The Crystal Structure of the Novobiocin Biosynthetic Enzyme NovP : The First Representative Structure for the TylF O -Methyltransferase Superfamily. *J. Mol. Biol.* **2010**, *395*, 390−407.
(41) Bernard, S. M.; Akey, D. L.; Tripathi, A.; Park, S. R.; Konwerski, J. R.; Anzai, Y.; Li, S.; Kato, F.; Sherman, D. H.; Smith, J. L. Structural Basis of Substrate Specificity and Regiochemistry in the MycF/TylF Family of Sugar O-Methyltransferases. *ACS Chem. Biol.* **2015**, *10*, 1340−1351.
(42) Bruender, N. A.; Thoden, J. B.; Kaur, M.; Avey, M. K.; Holden, H. M. Molecular Architecture of a C-3'-Methyltransferase Involved in the Biosynthesis of D-Tetronitrose. *Biochemistry* **2010**, *49*, 5891−5898.
(43) Carney, A. E.; Holden, H. M. Molecular Architecture of TylM1 from Streptomyces Fradiae: An N,N-Dimethyltransferase Involved in the Production of DTDP-D-Mycaminose. *Biochemistry* **2011**, *50*, 780−787.

https://doi.org/10.1021/acscatal.2c04240
ACS Catal. 2022, 12, 14130−14139